Discrete Adjoint-Based Aerodynamic Shape Optimization Framework for Natural Laminar Flows

Halil Kaya[*]
Turkish Aerospace Industries, Inc., 06980 Ankara, Turkey
and
İsmail H. Tuncer[†]
Middle East Technical University, 06800 Ankara, Turkey

An adjoint-based aerodynamic shape optimization framework for natural laminar flows is developed. The laminar to turbulent-transition onset is predicted by the correlation-based Bas–Cakmakcioglu transition model that is coupled with the Spalart–Allmaras turbulence model. A discrete adjoint implementation is subsequently developed. Automatic differentiation is utilized to construct the partial derivatives in the discrete adjoint formulation. The turbulence and transition models are fully coupled into the sensitivity derivative evaluations, as well as into the objective function evaluations. The sensitivity derivatives evaluated by the discrete adjoint solver are validated against those of the finite central difference method. The discrete adjoint-based aerodynamic shape optimization framework developed for natural laminar flows is successfully employed to optimize aerodynamic characteristics of the NLF(1)-0416 airfoil and a low-aspect-ratio wing.

Nomenclature

c	=	chord
c_d, C_D	=	drag coefficients of a two-dimensional airfoil and a three-dimensional wing, respectively
c_f	=	skin-friction coefficient
c_l, C_L	=	lift coefficients of a two-dimensional airfoil and a three-dimensional wing, respectively
c_p	=	pressure coefficient
d_w	=	distance to the closest wall boundary
e	=	unit vector
h	=	finite difference step size
I	=	objective function
J	=	augmented objective function
k	=	turbulent kinetic energy
M	=	Mach number
N_{cell}	=	number of cells
N_{dim}	=	dimension size
N_{node}	=	number of nodes
R	=	vector of governing equations
Re	=	Reynolds number
Re_ν	=	vorticity Reynolds number
Re_θ	=	momentum thickness Reynolds number
Re_{θ_c}	=	critical momentum thickness Reynolds number
T_{u_∞}	=	freestream turbulence intensity
t	=	thickness
U	=	flow variable
$\hat{U}$	=	a subset of flow variables
V	=	velocity magnitude
w	=	design variables
X	=	grid node coordinates
$\hat{X}$	=	a subset of grid node coordinates
y^+	=	nondimensional wall distance
α	=	angle of attack
γ_{BC}	=	Bas–Cakmakcioglu intermittency distribution function
η	=	half-span ratio
λ	=	adjoint vector
μ	=	dynamic viscosity
ν_{BC}	=	Bas–Cakmakcioglu turbulent kinematic viscositylike term
ν_t	=	turbulent kinematic viscosity
ρ	=	density
χ_1, χ_2	=	the first and second constants of the Bas–Cakmakcioglu transition model
Ω	=	vorticity

I. Introduction

IN MODERN days, fuel efficiency is of importance in the aviation industry more than ever. Notably, the increasing concerns regarding climate change push engineers to develop environmentally responsible designs by increasing fuel efficiency. One of the key technologies considered to increase fuel efficiency, and hence to reduce the environmental impacts of the aerial vehicles, is natural laminar flow (NLF) technology. Although, in the past, the NLF technology was primarily used on experimental aircraft and sailplanes, nowadays, thanks to high-fidelity transition prediction methods, NLF is finding its way onto long-endurance unmanned aerial vehicles, commercial aircraft, and business jets [1–4].

To properly benefit from NLF technology, engineers are supposed to support their design process with an aerodynamic shape optimization (ASO) study regarding the laminar to turbulent transition. Furthermore, in the design optimization of competitive modern aerial vehicles, a design engineer should use a large number of design variables that provide sufficient design flexibility. The optimization algorithm instrumented in the study should therefore be able to deal with a large number of design variables required by the optimum aerodynamic shape design efficiently.

Gradient-based optimization algorithms are widely employed in aerodynamic shape optimization studies. Although gradient-free and surrogate-based optimization algorithms are both successful in achieving the optimum design, they both face the curse of dimensionality when dealing with a large number of design variables. This means the number of flow analyses required by the method grows exponentially with the increasing number of design variables. Even though modern computers and computational fluid dynamics software packages enable the conduction of high-fidelity analysis within hours, gradient-free algorithms may still be infeasible to use in an

*Flight Mechanics Senior Specialist Engineer, Unmanned Aerial Vehicle Group; hkaya@tai.com.tr.

†Professor, Aerospace Engineering Department; ismail.h.tuncer@ae.metu.edu.tr.

optimization problem with a large number of design variables. On the other hand, gradient-based algorithms do not scale with the dimension of the problem exponentially and are more feasible in a large dimensional aerodynamic shape optimization problem [5,6].

The remaining task is to find an efficient way to compute the necessary sensitivity derivatives. Traditionally, the estimation of the sensitivity derivatives required in an optimization study is performed by the finite difference approximation. In the case of employing the finite difference approximation in a gradient-based algorithm, the computational cost of the algorithm is still much lower than the gradient-free and the surrogate-based optimization algorithms. Nevertheless, the dependence of the dimensionality abides, and an optimization problem still scales linearly with the number of design variables. The adjoint-based methods [7–10] developed recently have overcome this linear dependence of the numerical cost on the number of design variables. They accomplish the computation of sensitivity derivatives of a single engineering observation to a large number of design variables in a single computation. Therefore, an efficient method to conduct a high-fidelity ASO, which considers laminar to turbulent transition, is an adjoint-based optimization method with turbulence and transition models.

In the literature, there are some studies regarding adjoint-based optimization methods with turbulence and transition models. For instance, Khayatzadeh and Nadarajah [11,12] developed a discrete adjoint solver for the $k - w$ shear-stress transport turbulence model coupled with the $\gamma - Re_\theta$ transition model [13]. In their studies, they also carried out optimization studies to minimize the drag coefficients of S809, NACA 0012, and NLF(1)-0416 airfoils by minimizing turbulent kinetic energy k in the domain at a constant lift. Moreover, they optimized the c_l/c_d ratios of NACA 0012 and NLF(1)-0416 airfoils. Rashad and Zingg [14] developed a two-dimensional discrete adjoint solver for the Spalart–Allmaras turbulence model coupled with an e^n transition model. They conducted single-point and multipoint optimization studies on NLF airfoils by computing necessary derivatives with their discrete adjoint solver. Yang and Mavriplis [15] published an implementation of the adjoint solver for fully coupled turbulence-transition equations. They optimized a NACA 0012 airfoil in viscous flow with free transition to decrease drag and increase the c_l/c_d ratio. In the study, the turbulence model was the Spalart–Allmaras model; and the transition was modeled through the amplification factor transport equation [16]. Lee and Jameson [17] described an adjoint-based method for natural laminar flow airfoils and wings. However, in their study, the gradients computed by the adjoint method did not account for the transition prediction; and it is mainly focused on eliminating the shock waves. More recently, Pederson et al. [18] developed an approach for the design of vortex generators. The design optimization aimed to delay the transition by reducing the amplification of Mack mode instabilities for hypersonic boundary layers. Nevertheless, they did not integrate the transition analysis in their shape optimization study.

Although there are studies that combine NLF and adjoint methods, either these studies are limited to two-dimensional problems or the gradients computed by the adjoint method do not account for the transition. In the present study, the aim is to develop an adjoint-based optimization framework accounting for laminar to turbulent transition and to show the success of the framework in optimizing a wing, as well as an NLF airfoil.

II. Methodology

In the present study, an in-house flow solver is first extended to incorporate the Bas–Cakmakcioglu (B-C) transition model [19] in order to predict laminar to turbulent-transition onset. An associated adjoint solver is then developed by making use of an automatic differentiation tool, *TAPENADE* [20]. The flow solver and the developed adjoint solver are finally integrated into an optimization framework driven by an open-source software environment, *Dakota* [21].

A. Reynolds-Averaged Navier–Stokes Flow Solver

The flow solver used is an in-house flow solver developed by the Middle East Technical University's Aerospace Engineering Department. The flow solver is a finite volume, unstructured cell-centered density-based solver for both two-dimensional and three-dimensional flows governed by Reynolds-averaged Navier–Stokes (RANS) equations. The flow solver deals with both steady and unsteady flows. The temporal discretization scheme is a third-order explicit Runge–Kutta scheme. A local time-stepping scheme may also be employed in order to accelerate the convergence rate. The evaluation of gradients that is required for both viscous fluxes and second-order spatial accuracy is accomplished by the Green–Gauss approach or the inverse-distance weighted least-square approach. The convective fluxes are computed using a Riemann solver [22] that is a combination of the Roe's solver and the Rusanov/Harten–Lax–van Leer scheme. To get a physically relevant nonunique solution, Harten et al.'s entropy fix [23] is imposed. The viscous fluxes are discretized using central discretization. The closure of viscous RANS equations is achieved by the Spalart–Allmaras (S-A) turbulence model [24]. The turbulence model is made fully coupled with the main flow equations. Furthermore, the flow solver is parallelized by using the application programming interface Open multi-processing for shared memory systems. The detailed information of the in-house flow solver can be found in Ref. [25].

B. Transition Prediction

The laminar to turbulent-transition onset prediction has a crucial role in the NLF design. Therefore, it is necessary to employ a transition onset prediction method. There are various transition prediction models that may be categorized by whether they rely on nonlocal and local flow variables. The nonlocal models, such as the ones based on the parabolized stability equation, solve a nonlinear stability equation and require some integrated parameters and nonlocal flow information, such as the displacement and momentum thicknesses. An elaborate initialization is also required. They are still considered as costly and impractical to use for complex geometries. Yet recently, there are encouraging studies where a methodology with an automated initialization procedure is developed [26] and the solution efficiency is improved [27]. On the other hand, models based on local flow variables elude all the complications of the nonlocal methods and can easily be implemented. The $\gamma - Re_\theta$ and γ transition models by Menter et al. [13,28], the $k - k_L - \omega$ model by Walters and Leylek [29], and the Wray–Agarwal-γ two-equation transition model [30] are well-known local models. In the present study, the correlation-based algebraic Bas–Cakmakcioglu transition model developed recently is used. Since it is an algebraic model, it does not have any additional equation to be solved, which makes the model computationally efficient and easy to implement.

The B-C transition model employs an intermittency factor γ_{BC} to suppress the production of turbulence in laminar and transitional flow regions. The intermittency factor is multiplied by the turbulence production term of the S-A model. Until the transition onset criterion is satisfied, the intermittency factor has a value of zero, which means the production of the turbulence is prevented. Once the transition criterion is achieved, the intermittency factor gets a value higher than zero, hence transitional flow; subsequently, the turbulent flow starts.

In the model, the production of turbulence starts when locally computed momentum thickness Reynolds number Re_θ exceeds the critical momentum Reynolds number Re_{θ_c}. The critical value is determined by three different empirical relations: each of which corresponds to a different turbulence intensity range. The first transition onset correlation valid for $T_{u_\infty} < 1\%$ is as given in the study of Menter et al. [13]. The correlation is defined as

$$Re_{\theta c} = 803.73(T_{U_\infty} + 0.6067)^{-1.027} \tag{1}$$

The second correlation is similar to the relation stated in the study of Abu-Ghannam and Shaw [31]. The relation is used for $1\% \leq T_{u_\infty} \leq 3\%$. The correlation is defined as

$$Re_{\theta c} = 163 + e^{(6.91 - T_{U_\infty})} \tag{2}$$

The final correlation that determines the critical momentum Reynolds number is valid when $T_{u_\infty} > 3\%$. It was given by Mayle [32]. The correlation is stated as

$$Re_{\theta c} = 400 T_{U_\infty}^{-0.625} \tag{3}$$

The local value of the intermittency factor is evaluated by the relation given as

$$\gamma_{BC} = 1 - e^{(-\sqrt{\mathrm{Term}_1} - \sqrt{\mathrm{Term}_2})} \tag{4}$$

In Eq. (4), Term_1 stands for the prevention of turbulence production until the transition criterion is achieved. Moreover, it provides an artificial transition region between the laminar and turbulent regions. Term_1 is defined as

$$\mathrm{Term}_1 = \frac{\max(Re_\theta - Re_{\theta c}, 0, 0)}{\chi_1} \tag{5}$$

where

$$Re_\theta = \frac{Re_v}{2.193} \quad \text{and} \quad Re_v = \frac{\rho d_w^2}{\mu}\Omega \tag{6}$$

In Eq. (6), d_w denotes the closest distance to a wall boundary, and Ω denotes vorticity. In the original paper of the transition model, it is stated that Term_1 is not enough to model turbulence generation inside the boundary layer. That is because Re_v is inversely proportional to the square of the closest wall distance, and it gets quite a low value in the vicinity of the wall. To alleviate this issue, a new term, Term_2, is introduced. The term allows intermittency produced by Term_1 to penetrate the boundary layer. Term_2 is defined as

$$\mathrm{Term}_2 = \frac{\max(\nu_{BC} - \chi_2, 0.0)}{\chi_2} \tag{7}$$

where ν_{BC} is turbulent viscosity scaled with the local velocity magnitude V and the distance to the nearest wall d_w:

$$\nu_{BC} = \frac{\nu_t}{V d_w} \tag{8}$$

Note that χ_1 and χ_2 are the calibration constants of the model, and they are determined as

$$\chi_1 = 0.002 \quad \text{and} \quad \chi_2 = 5.0/Re \tag{9}$$

It should be noted that χ_2 is given as 5.0 in Ref. [19]. However, it is coded as $5.0/Re$ in the source code [33] of the open-source SU2 software suite [34], and it is corrected as $5.0/Re$ in the recent publications by Cakmakcioglu et al. [35] and Mura and Cakmakcioglu [36]. In addition, the transition model does not account for crossflow instabilities and should not be used in the simulation of swept natural laminar flow wings.

C. Discrete Adjoint Solver

In an aerodynamic shape optimization problem, an objective function I such as C_L or C_D depends on the geometric variables $\boldsymbol{w}$ that define the aerodynamic surfaces and the flowfield $\boldsymbol{U}$:

$$I = I(\boldsymbol{w}, \boldsymbol{U}(\boldsymbol{w})) \tag{10}$$

A subset of geometric variables $\boldsymbol{w}$, which define the aerodynamic surface to be optimized, is usually taken as the design variables. Since all the flow variables in the solution domain $\boldsymbol{U}$ depend on the geometric variables through the boundary conditions, the governing equations of flow that are in the RANS equations in the present study now become the constraints of the aerodynamic shape optimization problem:

$$\boldsymbol{R} = \boldsymbol{R}(\boldsymbol{w}, \boldsymbol{U}(\boldsymbol{w})) = 0 \tag{11}$$

By using a Lagrange multiplier to enforce the governing equations as constraints, an augmented objective function J may be introduced:

$$J = I(\boldsymbol{w}, \boldsymbol{U}(\boldsymbol{w})) + \lambda^T \boldsymbol{R}(\boldsymbol{w}, \boldsymbol{U}(\boldsymbol{w})) \tag{12}$$

The sensitivity of the augmented objective function to the design variables may be expressed as follows:

$$dJ = \frac{\partial I}{\partial \boldsymbol{U}} d\boldsymbol{U} + \frac{\partial I}{\partial \boldsymbol{w}} d\boldsymbol{w} + \lambda^T \left(\frac{\partial \boldsymbol{R}}{\partial \boldsymbol{U}} d\boldsymbol{U} + \frac{\partial \boldsymbol{R}}{\partial \boldsymbol{w}} d\boldsymbol{w} \right) \tag{13}$$

when the equation is regrouped as

$$dJ = \left(\frac{\partial I}{\partial \boldsymbol{U}} + \lambda^T \frac{\partial \boldsymbol{R}}{\partial \boldsymbol{U}} \right) d\boldsymbol{U} + \left(\frac{\partial I}{\partial \boldsymbol{w}} + \lambda^T \frac{\partial \boldsymbol{R}}{\partial \boldsymbol{w}} \right) d\boldsymbol{w} \tag{14}$$

To avoid the evaluation of $d\boldsymbol{U}$, its coefficient may be set to zero, which provides the well-known adjoint equation:

$$\frac{\partial I}{\partial \boldsymbol{U}} + \lambda^T \frac{\partial \boldsymbol{R}}{\partial \boldsymbol{U}} = 0 \Rightarrow \left[\frac{\partial \boldsymbol{R}}{\partial \boldsymbol{U}} \right]^T \lambda = - \left[\frac{\partial I}{\partial \boldsymbol{U}} \right]^T \tag{15}$$

The sensitivities are then obtained by the following equation:

$$\frac{dJ}{d\boldsymbol{w}} = \frac{dI}{d\boldsymbol{w}} = \frac{\partial I}{\partial \boldsymbol{w}} + \lambda^T \frac{\partial \boldsymbol{R}}{\partial} \tag{16}$$

In the adjoint method, the computational cost to solve the linear system given in Eq. (15) scales with the number of objective functions. Typically, aerodynamic shape optimization problems consider a single or a few objective functions like C_L/C_D, $C_L^{3/2}/C_D$, etc. However, the shape is generally defined and controlled by tens or hundreds of design variables. Hence, the adjoint method provides a prominent computational advantage in dealing with aerodynamic shape optimization problems.

It should be noted that the governing equations $\boldsymbol{R}$ and the objective function value I are also functions of grid coordinates $\boldsymbol{X}$. Thus, Eq. (16) may be rewritten as

$$\frac{d}{d\boldsymbol{X}} \frac{d\boldsymbol{X}}{d\boldsymbol{w}} = \left(\frac{\partial I}{\partial \boldsymbol{X}} + \lambda^T \frac{\partial \boldsymbol{R}}{\partial \boldsymbol{X}} \right) \frac{d\boldsymbol{X}}{d\boldsymbol{w}} \tag{17}$$

In the present study, the sensitivity derivatives of the objective function with respect to grid coordinates and the sensitivity derivatives of the grid coordinates with respect to the design variables are computed separately. The sensitivities of the objective function with respect to design variables are then computed by performing the dot product given in Eq. (17).

In the present study, an automatic differentiation (AD) [37,38] tool based on source transformation, TAPENADE, is selectively used in the forward mode to evaluate the partial derivatives appearing in the adjoint formulation [Eqs. (15) and (16)]. The approach employed to evaluate the partial derivatives is similar to the approach proposed by Mader et al. [39], with some differences in the implementation.

1. Computation of Flux Jacobian Matrices

Note that the $\partial \boldsymbol{R}/\partial \boldsymbol{U}$ term in the adjoint system of equations, which is known as the flux Jacobian matrix, contains the partial sensitivity of the governing equations for a cell $\boldsymbol{R}$ with respect to all flow variables $\boldsymbol{U}$. The matrix is of the dimension $N_U N_{\mathrm{cell}} \times N_U N_{\mathrm{cell}}$, where N_U is the number of the flow variables and N_{cell} is the number of cells in the computational domain. The flux Jacobian matrix $\partial \boldsymbol{R}/\partial \boldsymbol{U}$ is given as in Eq. (18). Note that, in a turbulent flow case, $\boldsymbol{R}$ includes the Spalart–Allmaras eddy viscosity model, and $\boldsymbol{U}$ similarly includes the working variable of the turbulence model:

$$
\begin{bmatrix}
\dfrac{R_{1,1}}{\partial U_{1,1}} & \dfrac{R_{1,1}}{\partial U_{1,1}} & \cdots & \dfrac{\partial R_{1,1}}{\partial U_{N_U,1}} & \dfrac{\partial R_{1,1}}{\partial U_{1,2}} & \cdots & \dfrac{\partial R_{1,1}}{\partial U_{N_U,N_{cell}}} \\[8pt]
\dfrac{\partial R_{2,1}}{\partial U_{1,1}} & \dfrac{\partial R_{2,1}}{\partial U_{2,1}} & \cdots & \dfrac{\partial R_{2,1}}{\partial U_{N_U,1}} & \cdots & & \dfrac{\partial R_{2,1}}{\partial U_{N_U,N_{cell}}} \\[8pt]
\vdots & \vdots & \cdots & \vdots & \cdots & & \vdots \\[8pt]
\dfrac{\partial R_{N_U,1}}{\partial U_{1,1}} & \dfrac{\partial R_{2,1}}{\partial U_{1,1}} & \cdots & \dfrac{\partial R_{2,1}}{\partial U_{1,1}} & \cdots & & \dfrac{\partial R_{N_U,1}}{\partial U_{N_U,N_{cell}}} \\[8pt]
\dfrac{\partial R_{1,2}}{\partial U_{1,1}} & \vdots & \vdots & \vdots & \ddots & & \dfrac{\partial R_{1,2}}{\partial U_{N_U,N_{cell}}} \\[8pt]
\vdots & & & & & \ddots & \vdots \\[8pt]
\dfrac{\partial R_{N_U,N_{cell}}}{\partial U_{1,1}} & \dfrac{\partial R_{N_U,N_{cell}}}{\partial U_{2,1}} & \cdots & \dfrac{\partial R_{N_U,N_{cell}}}{\partial U_{N_U,1}} & \dfrac{\partial R_{N_U,N_{cell}}}{\partial U_{1,2}} & \cdots & \dfrac{\partial R_{N_U,N_{cell}}}{\partial U_{N_U,N_{cell}}}
\end{bmatrix}
\quad (18)
$$

The first subscript of R refers to the governing equations: the conservation of mass, momentum, energy, and the turbulence model, respectively. The second subscript of R denotes the cell index. The first subscript of U denotes the flow variable, and the second subscript denotes the cell index.

The flux Jacobian matrix, $\partial R / \partial X$, in Eq. (17) contains the partial derivatives of the governing equations R with respect to the coordinates of the grid node coordinates X. The dimension of the matrix is $N_U N_{cell} \times N_{dim} N_{node}$, where N_{dim} and N_{node} stand for the dimension of the problem and the number of grid nodes in the computational domain, respectively. The flux Jacobian matrix, $\partial R / \partial X$, is given as

$$
\begin{bmatrix}
\dfrac{\partial R_{1,1}}{\partial X_{1,1}} & \cdots & \dfrac{\partial R_{1,1}}{\partial X_{N_{dim},1}} & \dfrac{\partial R_{1,1}}{\partial X_{1,2}} & \cdots & \cdots & \dfrac{\partial R_{1,1}}{\partial X_{N_{dim},N_{node}}} \\[8pt]
\dfrac{\partial R_{2,1}}{\partial X_{1,1}} & \cdots & \dfrac{\partial R_{2,1}}{\partial X_{N_{dim},1}} & \dfrac{\partial R_{2,1}}{\partial X_{1,2}} & \cdots & & \dfrac{\partial R_{2,1}}{\partial X_{N_{dim},N_{node}}} \\[8pt]
\vdots & \vdots & \vdots & \vdots & \cdots & & \vdots \\[8pt]
\dfrac{\partial R_{N_U,1}}{\partial X_{1,1}} & \cdots & \dfrac{\partial R_{N_U,1}}{\partial X_{N_{dim},1}} & \dfrac{\partial R_{N_U,1}}{\partial X_{1,2}} & \cdots & & \dfrac{\partial R_{N_U,1}}{\partial X_{N_{dim},N_{node}}} \\[8pt]
\dfrac{\partial R_{1,2}}{\partial X_{1,1}} & \cdots & \vdots & \vdots & \ddots & \cdots & \dfrac{\partial R_{1,2}}{\partial X_{N_{dim},N_{node}}} \\[8pt]
\vdots & \vdots & & & & \ddots & \vdots \\[8pt]
\dfrac{\partial R_{N_U,N_{cell}}}{\partial X_{1,1}} & \cdots & \dfrac{\partial R_{N_U,N_{cell}}}{\partial X_{N_{dim},1}} & \dfrac{\partial R_{N_U,N_{cell}}}{X_{1,2}} & \cdots & \cdots & \dfrac{\partial R_{N_U,N_{cell}}}{\partial X_{N_{dim},N_{node}}}
\end{bmatrix}
\quad (19)
$$

As is in the $\partial R / \partial U$ expression, the first subscript of R denotes the governing equation, and the second subscript denotes the cell index. The first subscript of X denotes the x, y, and z coordinates, respectively; whereas the second subscript refers to the node index.

In the flow solver, the cell fluxes are computed by looping over all the cell faces. Therefore, before employing the AD tool to generate the modules that provide the partial derivatives needed in the adjoint formulation, a function that evaluates the governing equations for a single cell is recoded for compactness and numerical efficiency. This subroutine accepts a subset of the flow variables $\hat{U}$ and a subset of the node coordinates $\hat{X}$ involved in the discrete evaluation of the governing equations for a cell R_i. For a first-order scheme, $\hat{U}$ and $\hat{X}$ include the flow variable and the node coordinates of the cell and the neighboring cells, respectively. For a second-order scheme, they also include the flow variables and node coordinates of the cells that are the neighbors to the immediate neighbor cells. The other input arguments of the subroutine are either constant values or not explicitly dependent on the flow variables and the node coordinates. Therefore, the subroutine recomputes all intermediate variables required to compute R_i, such as turbulent viscosity, gradients of flow variables, face normals, the cell volumes, and the flow variables at a boundary face if there is an explicit dependence on the boundary face. As a result, the standalone subroutine includes all the functional relations between the input variables $\hat{U}$ and $\hat{X}$ as well as the output variable R_i.

The standalone subroutine is now used with the AD tool TAPENADE in order to generate a subroutine that computes the partial derivatives of the governing equations R_i of a cell with respect to a flow variable j of a dependent cell k, $U_{j,k}$. By calling the generated subroutine for each flow variable of each dependent cell, the partial derivatives of the discrete governing equations of a cell are computed. Similarly, when the subroutine is differentiated with respect to the grid node coordinates, TAPENADE applies the chain rule line by line and generates a subroutine that computes the partial derivatives of the governing equations for a cell i with respect to a coordinate m of a dependent node n, $\partial R_i / \partial X_{m,n}$. The elements of $\partial R_i / \partial X$ are computed by calling the subroutine for each coordinate of each dependent node. Finally, by looping over all the cells in the computational domain, the Jacobian matrices $\partial R / \partial U$ and $\partial R / \partial X$ are constructed. Since the governing equations for a cell only depend on a relatively small number of neighbor cells, the CPU time required to compute the Jacobian matrices is relatively short.

Note that the S-A model equation and the intermittency value appearing in the B-C transition model depend on wall distances, which cause an additional dependency of the governing equations on the wall distances. To simplify the construction of the Jacobian matrices, this dependence is removed by providing wall distances as constant arguments. Thus, the implicit relationship between the wall distances and the node coordinates is concealed. A similar approach was also applied for the dependency of the S-A model on wall distances in the study of Lyu et al. [40].

2. Computation of Partial Sensitivities of Objective Function

The computation of partial sensitivity of the objective function is accomplished by a similar approach applied to construct the flux Jacobian matrices. To generate the subroutines computing the partial derivatives of an objective function by using TAPENADE, first, a subroutine that defines all explicit relations between the contribution of a cell to the objective function I_i and a subset of flow variables $\hat{U}$ and node coordinates $\hat{X}$ on which I_i explicitly depends $[I_i(\hat{U}, \hat{X})]$ is written. $\hat{U}$ and $\hat{X}$ include the flow variables and grid node coordinates of neighboring cells (also next-neighboring cells, depending on the objective functions), respectively. Moreover, the other input arguments are either constant values or not explicitly dependent on flow variables or the grid. The subroutine performs all corresponding computations required to evaluate the contribution of a cell to the objective function I_i. AD is then employed to differentiate the subroutine with respect to grid node coordinates and the flow variables. In this way, the subroutines that evaluate the sensitivities of the objective function are created. Finally, the sensitivities to each grid node coordinate and each flow variable are evaluated by calling these subroutines.

The dimension of the vector, $\partial I / \partial U$, is $N_U N_{cell}$. The appearance of the vector is given in Eq. (20):

$$
\frac{\partial I}{\partial U} = \begin{bmatrix} \dfrac{\partial I}{\partial U_{1,1}} & \dfrac{\partial I}{\partial U_{2,1}} & \cdots & \dfrac{\partial I}{\partial U_{N_U,1}} & \dfrac{\partial I}{\partial U_{1,2}} & \cdots & \dfrac{\partial I}{\partial U_{N_{U-1},N_{cell}}} & \dfrac{\partial I}{\partial U_{N_U,N_{cell}}} \end{bmatrix} \quad (20)
$$

The partial sensitivity vector of an objective function with respect to grid node coordinates, $\partial I / \partial X$, is given in Eq. (21). The vector is in the dimension of $N_{dim} N_{node}$:

$$
\frac{\partial I}{\partial X} = \begin{bmatrix} \dfrac{\partial I}{\partial X_{1,1}} & \cdots & \dfrac{\partial I}{\partial X_{N_{dim},1}} & \dfrac{\partial I}{\partial X_{1,2}} & \cdots & \dfrac{\partial I}{\partial U_{N_{dim-1},N_{node}}} & \dfrac{\partial I}{\partial U_{N_{dim},N_{node}}} \end{bmatrix} \quad (21)
$$

In the present study, the objective functions are the functions of aerodynamic loads, such as C_L / C_D. However, it is possible to define any objective functions that are a function of flow variables or/and the grid, e.g., the total pressure recovery of an engine inlet.

3. Solution of Adjoint System of Equations

The computation of the partial derivatives is followed by the solution of the adjoint system given in Eq. (15). The sensitivity derivatives are then evaluated by Eq. (16).

Since the governing equations for a cell only depend on the cell itself and a small number of neighboring cells, the flux Jacobian matrix, $\partial R/\partial U$, is very sparse. To take advantage of the sparsity and solve the system efficiently, a very instrumental and efficient parallel sparse direct solver referred to as *MUMPS* (which stands for multifrontal massively parallel solver) [41,42] is used under the Portable Extensible Toolkit for Scientific Computation (known as *PETSc*) environment [43–45]. In the present study, due to its robustness and accuracy, a direct solver is employed to solve the adjoint system. However, the vast memory requirement due to fill-in during lower–upper decomposition may preclude the use of a direct solver. Therefore, relatively large problems may be solved using an iterative solver (e.g., Generalized minimal residual method) with a proper preconditioner.

The performance of the adjoint solver is evaluated in a parallel computing environment in terms of runtime and memory usage per node. The benchmark study is performed for a second-order-accurate three-dimensional turbulent flow case. The analysis is carried out in a Linux cluster having 24 nodes, where each compute node has two Intel Xeon® Gold 6148 processors with 20 cores running at a 2.4 GHz base clock speed and with 186 GB of memory. The runtime and average memory usage per node are given in Fig. 1. Furthermore, as a reference, the memory usage and runtime per iteration of the explicit flow solver for the same problem are also provided in Fig. 1.

Since the flow solver is parallelized for shared memory systems, the flow analyses are conducted on a single node. Note that a converged solution generally requires 50,000 to 300,000 iterations, depending on the problem.

D. Optimization Framework

The gradient-based optimization process is driven by the Dakota software environment. The framework uses the *SU2_DEF* and *SU2_DOT_AD* modules available in the open-source *SU2* software suite, the flow solver, and the adjoint solver.

The flow chart of the optimization process is depicted in Fig. 2. As shown in the figure, the baseline configuration and the corresponding computational grid are provided for the framework. The aerodynamic surface to be optimized is then parameterized by using a Free-Form Deformation (FFD) technique [46]. The optimization algorithm generates a new set of design variables w that are the node coordinates of the FFD box. The volume grid is then deformed through an approach based on the linear elasticity equation [47]. To reduce the cell deformations and keep the wall distances about the same within the boundary layers, the stiffness coefficients are made inversely proportional to the wall distance. The parametrization of the surface and the deformation of the grid is accomplished by the *SU2_DEF* module. The flow solver computes the value of the objective function, I, and the partial derivatives required by the adjoint solver. The adjoint
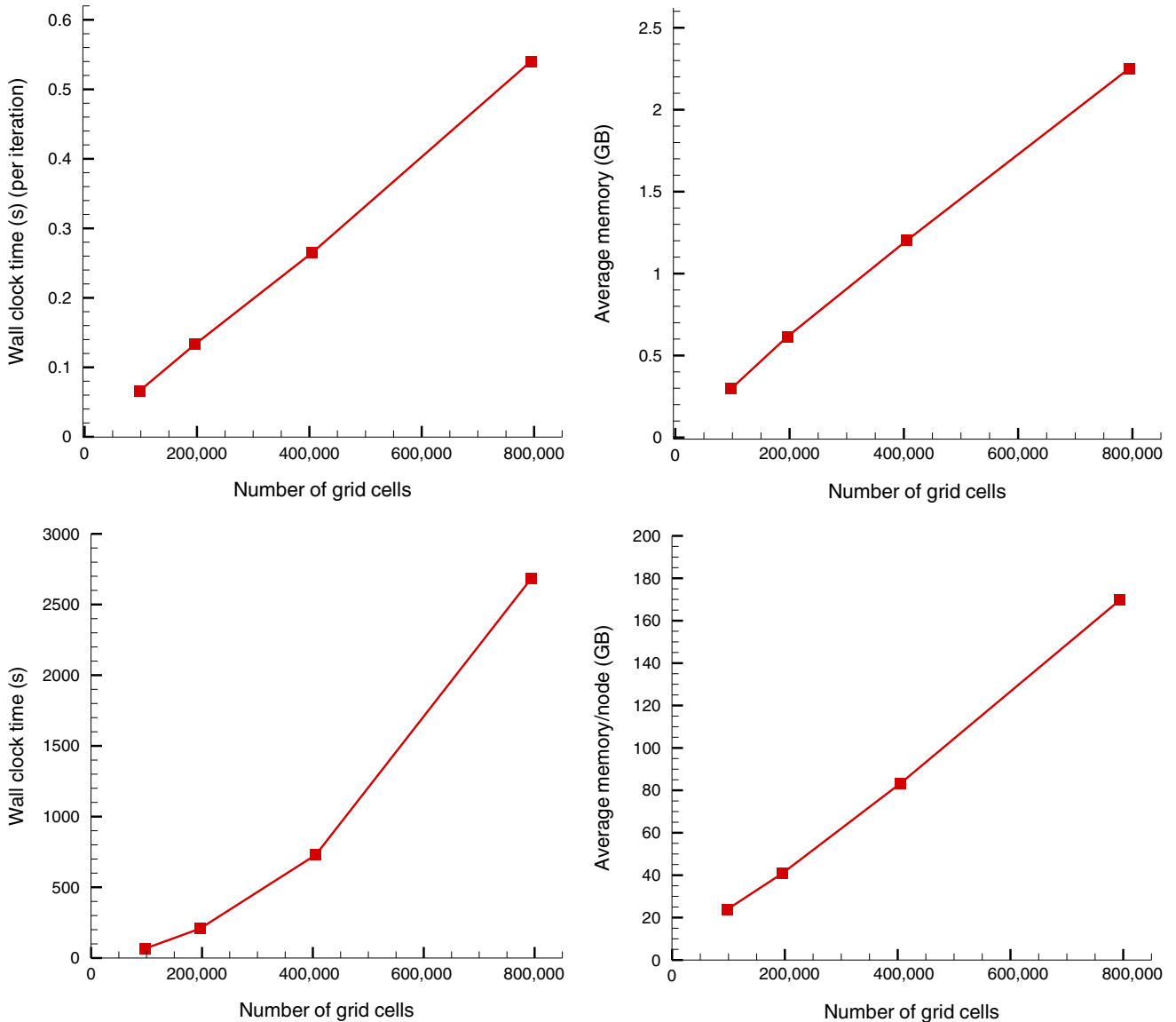

Fig. 1   Runtime and average memory usage per node of the flow solver (top) and the adjoint solver (bottom) vs number of grid cells.
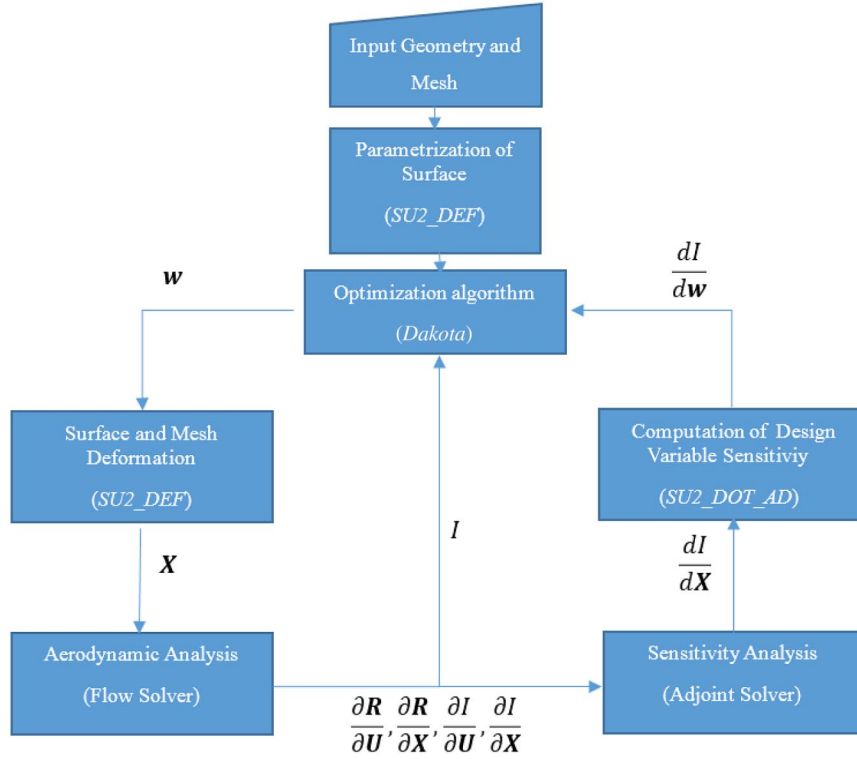
Fig. 2   Optimization flowchart.

solver firstly solves for the adjoint variables, then evaluates the grid sensitivities of the objective function, dI/dX. Finally, the sensitivities with respect to the design variables, dI/dw, are evaluated by the dot product given in Eq. (22). The computation of the grid sensitivities and the dot product is performed by $SU2\_DOT\_AD$.

$$\frac{dI}{dw} = \frac{dI}{dX}\frac{dX}{dw} \qquad (22)$$

The search for the optimum in Dakota is performed through the quasi-Newton method with a Broyden–Fletcher–Goldfarb–Shanno approximation to the Hessians [48–51]. The quasi-Newton algorithm employed in Dakota is the implementation of the OPT++ library [52]. As the stopping criterion in the optimization algorithm, a relative convergence tolerance of 0.0001 for the objective function is employed.

III.   Results and Discussion

Before the optimization studies, the validation of the flow solver and the adjoint solver in the framework is performed. In the validation studies, the NLF(1)-0416 airfoil and a low-aspect-ratio wing are considered. Following the validation studies, the same airfoil and the wing are optimized for the range and the endurance parameter, respectively.

A.   Validation of the Transition Model

1.   Flow over NLF(1)-0416 Airfoil

The accuracy and the capability of the flow solver developed are demonstrated by analyzing and then comparing the numerical and the experimental predictions for a natural laminar flow over the NLF(1)-0416 airfoil, for which there is an experimental study performed by Somers [53]. In the present study, the flow over the NLF(1)-0416 airfoil at a Mach number of 0.1 and a Reynolds number of 2×10^6 is considered. Since the inflow turbulent intensity is not given in the reference study [53], low-level turbulence is assumed; and it is set to 0.1%.

A grid convergence study is first conducted. To this end, a family of C-type computational grids is generated as given in Table 1 and

Table 1   Characteristics of grids

Grid level	Number of nodes on the airfoil	Grid size	y^+
1	120	240×80	1.0
2	200	360×100	0.6
3	280	560×140	0.2
4	400	720×200	0.1

shown in Fig. 3. The far-field boundary in all the grids is placed about 50 chord lengths away.

The lift and drag coefficients predicted on the computational grids are given in Fig. 4. The variation of the transition onset locations predicted on the computational grids is similarly compared in Fig. 5. The maximum deviations in the lift and drag coefficients between the results obtained using grid level 3 and level 4 are less than 0.001 and 0.0001, respectively. Moreover, the transition onset locations estimated using grid level 3 and level 4 are less than 1% of the chord length. Therefore, it is again concluded that grid level 3 (Fig. 3) provides a grid-independent solution

To validate the flow solver, the lift and drag coefficients and the transition onset locations predicted on the grid level 3 are compared with the experimental data. As shown in Fig. 6, the numerical predictions are in good agreement with the experimental data. The lift is predicted slightly higher, whereas the drag is predicted slightly lower. The deviation in the drag coefficient is not more than 12 drag counts, and the difference in the lift curve slope is less than 4%.

The transition locations predicted are compared to the experimental data in Fig. 7. In the experimental study, microphones connected to the orifices are used to detect the location of the boundary-layer transition from laminar to turbulent. The transition location is determined by measuring the noise level. In the laminar part, it is virtually silent, and an increase in noise level indicates the turbulent flow. Thus, the transition location can only be localized between two adjacent orifices, as shown in Fig. 7, where the empty symbols indicate the location of the last orifice on which the flow is laminar, and the solid symbols indicate the location of the first orifice on which the flow is turbulent.
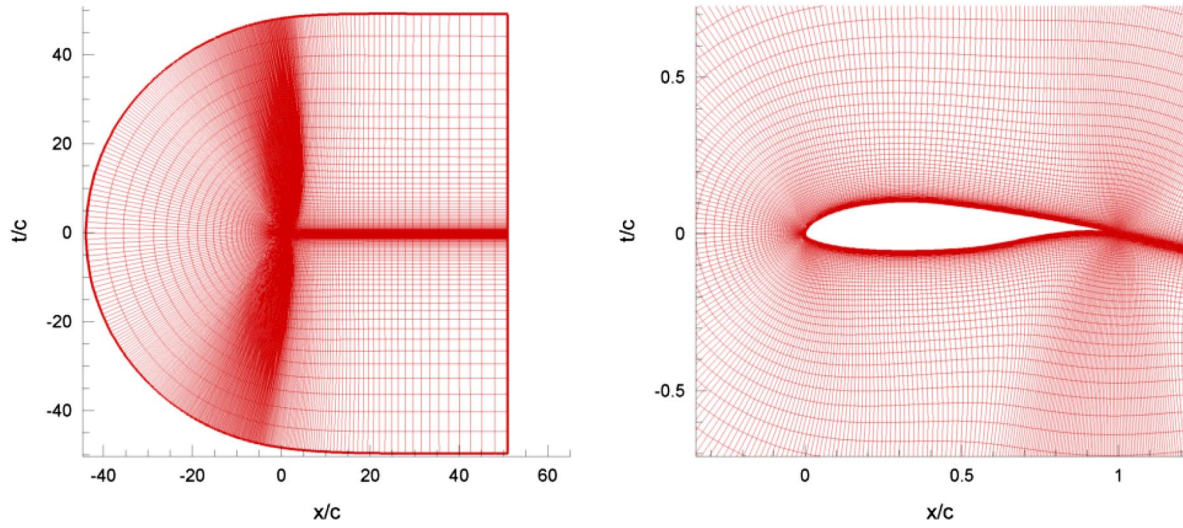
Fig. 3   Computational grid for NLF(1)-0416 airfoil (grid level 3).
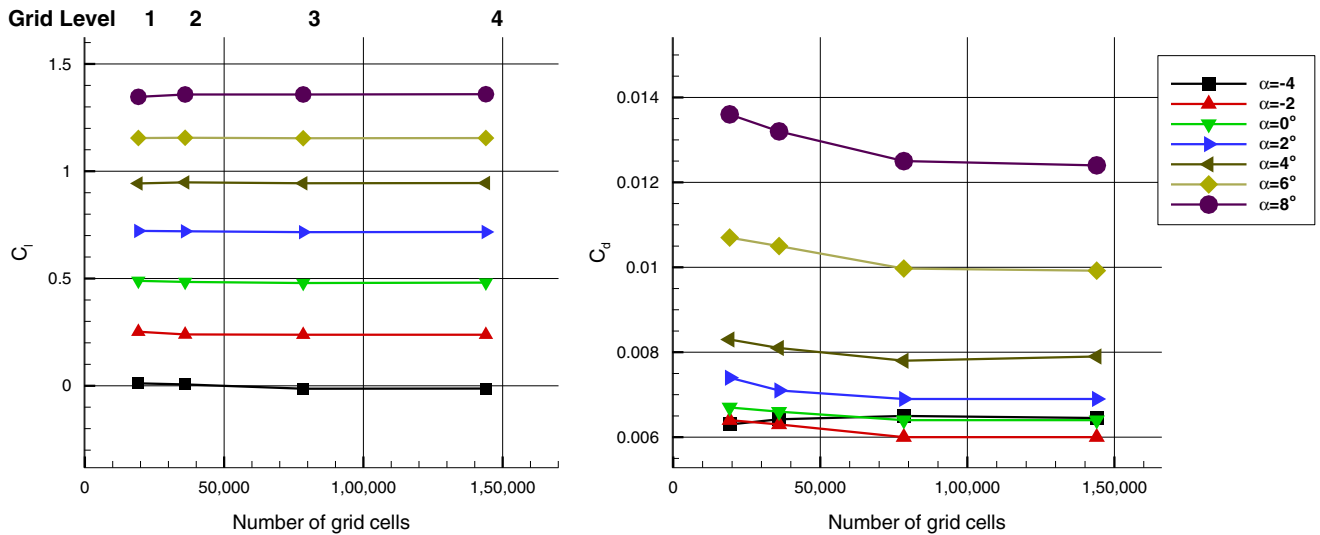

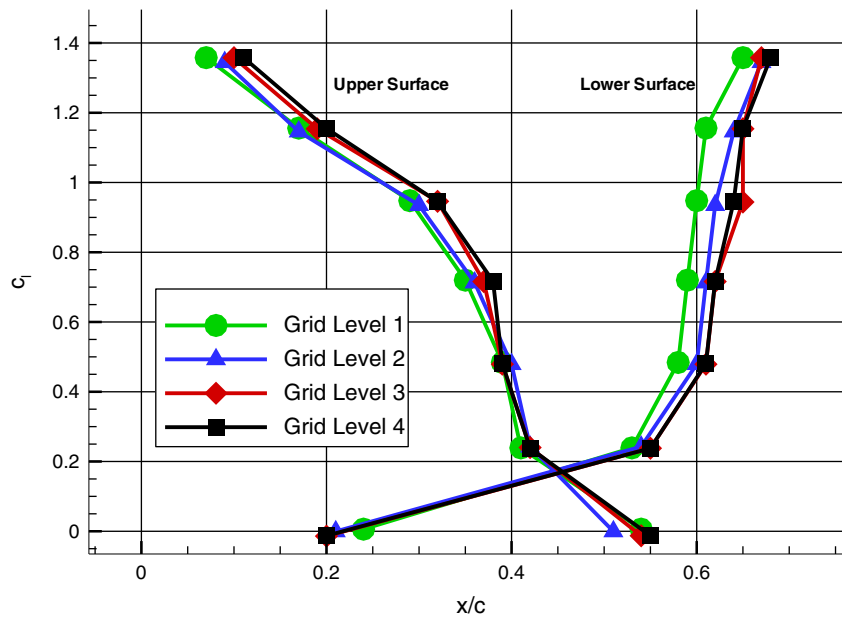**Fig. 4   Variation of lift and drag coefficients with different grid levels.**

Fig. 5   Transition onset locations predicted on different grid levels.
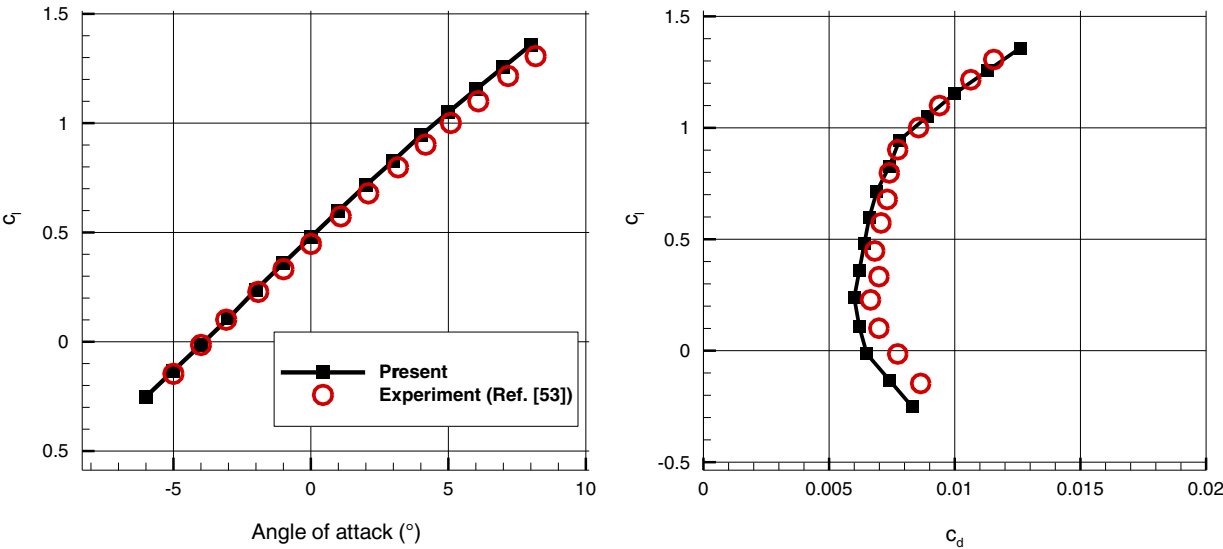
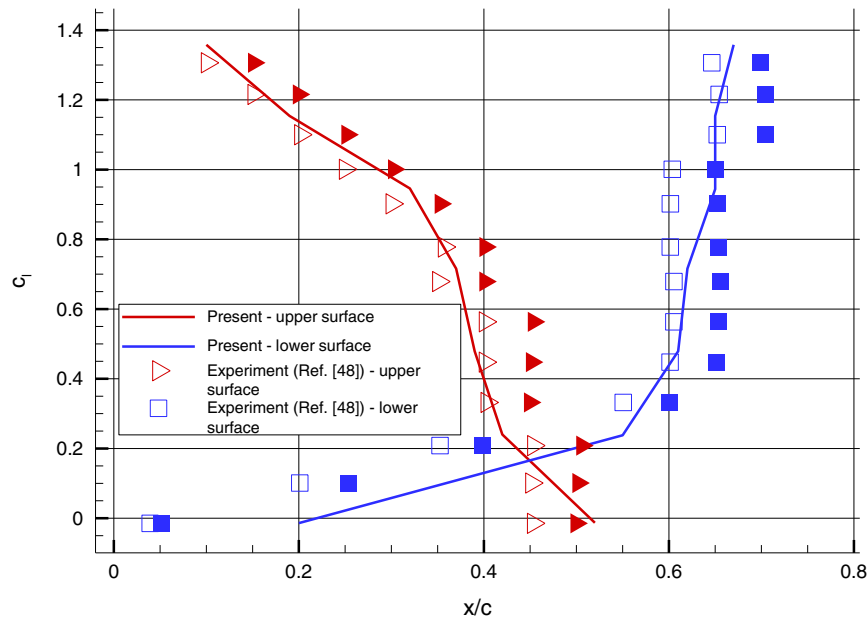**Fig. 6   Variation of the lift and drag coefficients.**

Fig. 7   Variation of transition location on airfoil surface. (Empty symbols indicate last orifices on which flow is laminar, and solid symbols indicate first orifices on which flow is turbulent.)

The transition onset locations predicted by the B-C transition model and measured in the experimental study are similarly in good agreement (Fig. 7). As the lift increases, the transition onset on the upper surface moves steadily forward. On the lower surface, it moves backward and reaches a terminal value of about 60% chord location beyond the lift coefficient value of 0.4.

2.   Flow over Low-Aspect-Ratio Wing

In this validation case, a low-aspect-ratio wing is considered. The wing model is based on a full-scale wingtip structure studied both experimentally and numerically within the framework of the international "the Consortium for Research and Innovation in Quebec Multi-Disciplinary Optimization (MDO) 505 Morphing Wing Project". In the experimental studies, the transition region is captured through infrared thermographic camera visualizations. More information regarding the project and the wind-tunnel test of the wing can be found in Refs. [54,55].

The geometric properties of the wing are given in Table 2, and the baseline wing section is illustrated in Fig. 8. Since the exact wingtip

Table 2   Geometrical properties of MDO 505 wing

Parameter	Value
Half-span length	1.5 m
Length of root length	1.5 m
Taper ratio	0.72
Aspect ratio	2.325
Leading-edge sweep angle	8 deg
Trailing-edge sweep angle	8 deg

model is not provided in Refs. [54,55], a rounded wingtip is used in the computations.

In this three-dimensional validation case, a grid-independence study is similarly performed using four levels of grids with increasing resolutions, as given in Table 3 and shown in Fig. 9.

The flow conditions considered, which are given in Table 4, are the first three cases studied in Ref. [55]. Turbulence intensity is set to
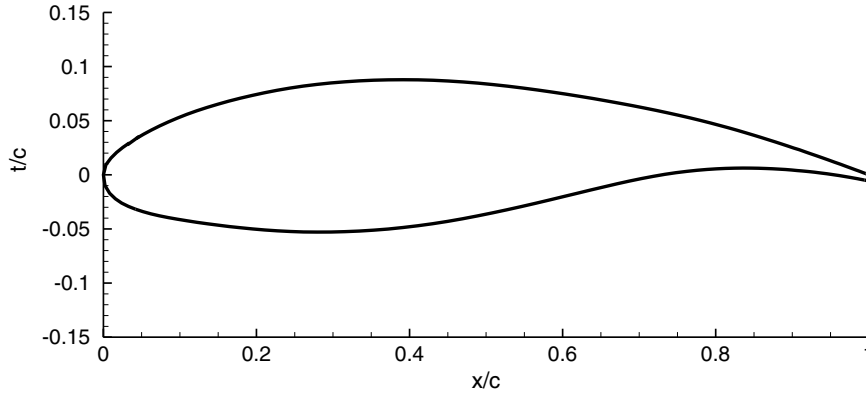
Fig. 8   Baseline wing section of MDO 505 morphing wing.

Table 3   Characteristics of grids for MDO 505 wing

Grid level	Number of cells on the wing	Number of cells	y^+
1	4,956	208,152	0.65
2	7,592	377,208	0.50
3	11,571	794,112	0,40
4	21,008	1,617,616	0.20

Table 4   Flow conditions

Case no.	M	Angle of attack, deg	Re, /m
1	0.15	0.68	3.4×10^6
2	0.15	1.5	3.4×10^6
3	0.15	2.1	3.4×10^6
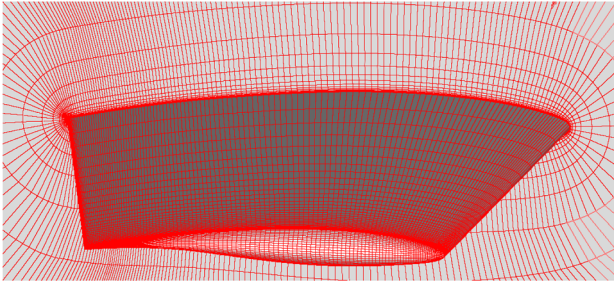
Fig. 9   Computational grid for MDO 505 wing (grid level 3).

0.14%, which is the value provided in Ref. [51]. The lift and drag coefficients obtained on all grid levels are depicted in Fig. 10.

The variation of transition onset locations at the midspan section predicted on the computational grids is similarly compared in Fig. 11. The maximum deviations between the results obtained using grid level 3 and level 4 are less than 0.001 and 0.0001 in

the lift and drag coefficients, respectively. The maximum deviation in the estimated transition onset locations is less than 1% of the chord length. So, it is concluded that grid level 3 provides a grid-independent solution.

For validation, in Fig. 12, the transition onset locations at the midspan section predicted by the numerical simulations in all three cases are compared with the experimental data. As observed, the maximum difference in the mean transition locations is about 6% of the chord length. Incidentally, a similar comparison with another numerical study is made in the reference study of Ref. [55], and it was concluded that a difference of less than 6% in the prediction of the transition location is considered acceptable.

B.   Validation of the Adjoint Solver

The methodology to validate the adjoint solver is the commonly used finite difference technique. In the study, the finite central difference approximation is used. The sensitivity derivatives are calculated by Eq. (23):
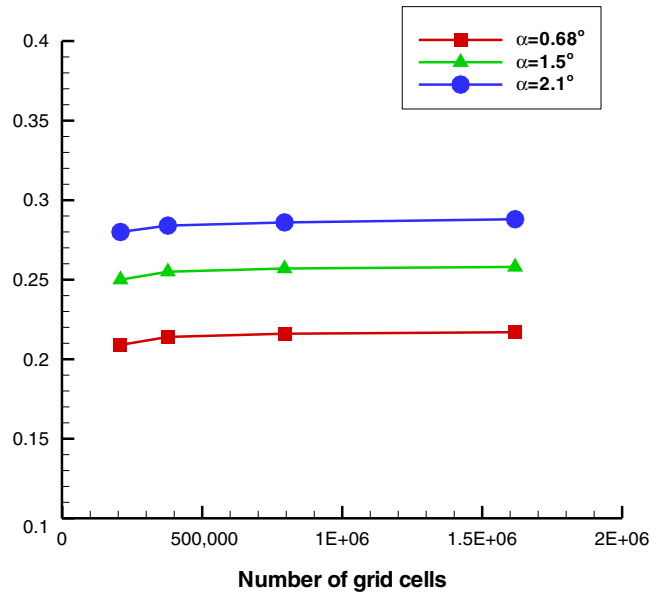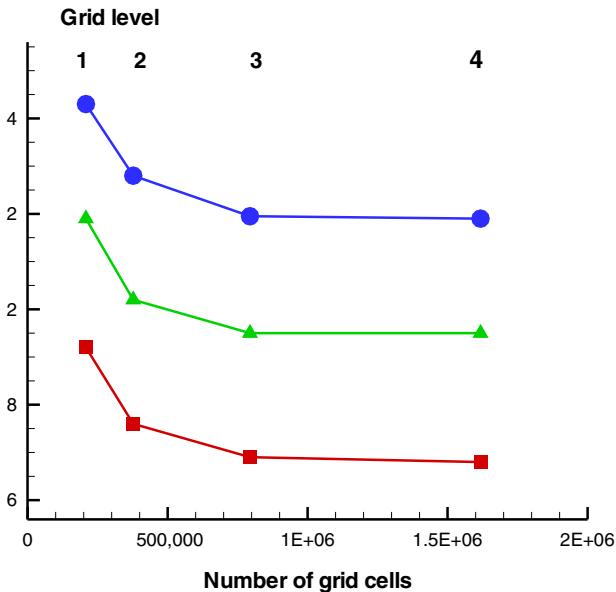

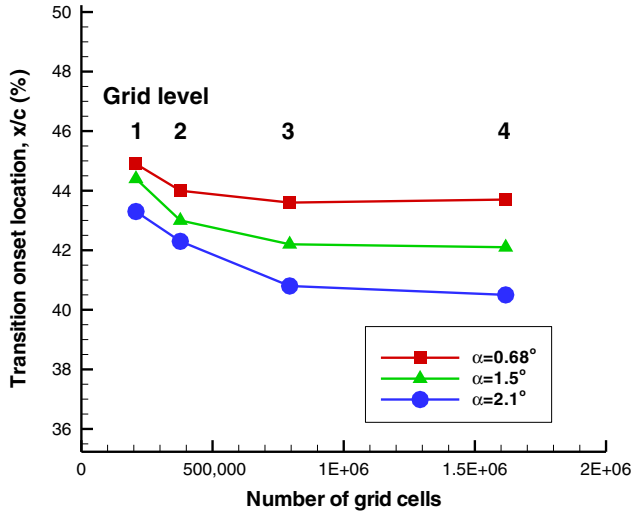**Fig. 10   Variation of lift and drag coefficients with different grid levels.**

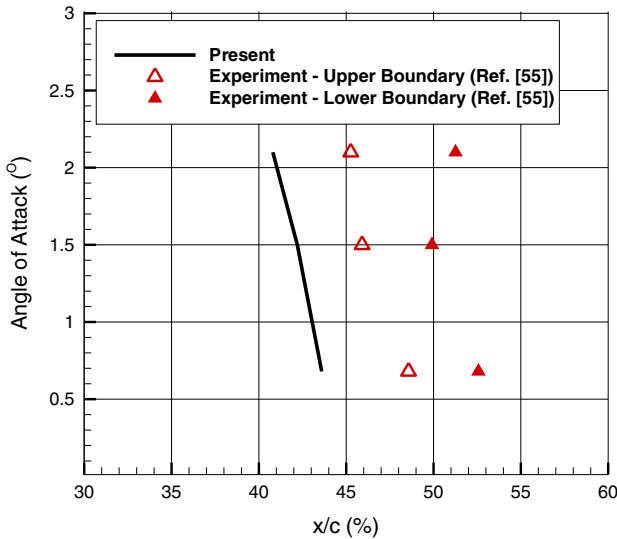**Fig. 11   Variation of transition onset at the midspan section with different grid levels.**

Fig. 12   Midspan transition onset locations in all three cases.

$$\frac{dI}{dw_i} = \frac{I(\boldsymbol{w}_0 + h\boldsymbol{e}_i) - I(\boldsymbol{w}_0 - h\boldsymbol{e}_i)}{2h} + \mathcal{O}(h^2) \qquad (23)$$

where $\boldsymbol{e}_i$ is the ith unit vector, and $\mathcal{O}(h^2)$ refers to a truncation error of approximation proportional to h^2. For an accurate approximation, the perturbation step size h should be chosen as small as possible to keep

the truncation error low, but not so small that the finite differences are in the noise. By the numerical experiments, the step size of 0.001 is chosen. The method compels performance of backward and a forward differencing for each design variable in order to compute sensitivity derivatives with respect to each design variable. Thus, two analyses are conducted for each design variable.

The sensitivity derivatives calculated by the finite central difference approximation are compared against the derivatives calculated by the adjoint solver. To validate the adjoint solver, the NLF(1)-0416 airfoil and the MDO 505 wing are considered.

1.   Range Parameter Sensitivity for NLF(1)-0416

The first validation case considers the flow over the NLF(1)-0416 airfoil at $Re = 2 \times 10^6$ and $M = 0.1$. In the case, the angle of attack is set to a value of 4.5 deg, at which the lift coefficient is 1.0. The same grid employed in the validation of the flow solver is used (Fig. 3).

The airfoil is parameterized by an FFD box with 22 control points, as illustrated in Fig. 13. The control points at the corners of the FFD box are fixed, and the remaining 18 control points whose movements are limited in the y direction are taken as the design variables.

The objective function stated in Eq. (24) is the lift-to-drag ratio (i.e., range parameter):

$$I = c_l/c_d \qquad (24)$$

The comparison of the sensitivity derivatives computed by the adjoint solver and the finite difference is shown in Fig. 14. As seen in the figure, the sensitivity derivatives computed by the adjoint solver agree well with the finite difference approximations, with the maximum deviation of 1.8% of the L_2 norm of the sensitivity derivatives computed by the finite difference approximation.

2.   Endurance Parameter Sensitivity for Low-Aspect-Ratio Wing

For the validation of the three-dimensional adjoint solver, the flow over an MDO 505 wing is considered at $\alpha = 2.1$ deg, $M = 0.15$, and $Re = 3.4 \times 10^6$ per meter. As in the previous case, the surface parametrization is achieved by the use of a three-dimensional FFD box. The FFD box and its control points employed are shown in Fig. 15. There are 36 control points, which define the upper and lower surfaces of the wing, and 24 of them are taken as the design variables. The control points are similarly allowed to move only in the vertical direction.

In this case, the endurance parameter given as follows is taken as the objective function:

$$I = C_L^{3/2}/C_D \qquad (25)$$

The sensitivity derivatives computed by the three-dimensional adjoint solver are developed, and the finite central difference approximations are shown in Fig. 16. Similar to the previous two-dimensional study, these two predictions are in very good agreement, with
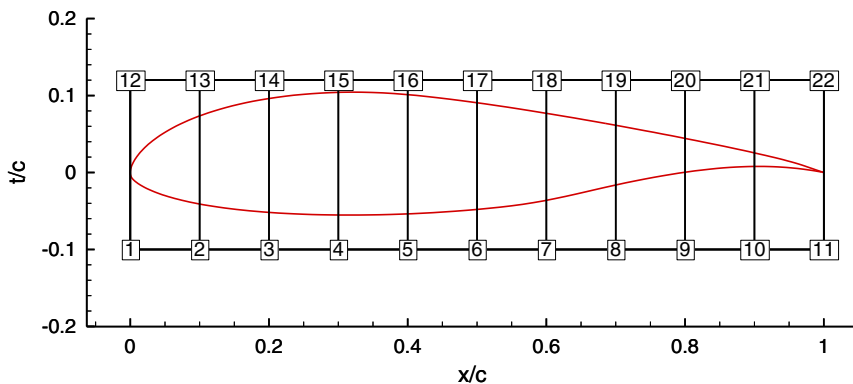

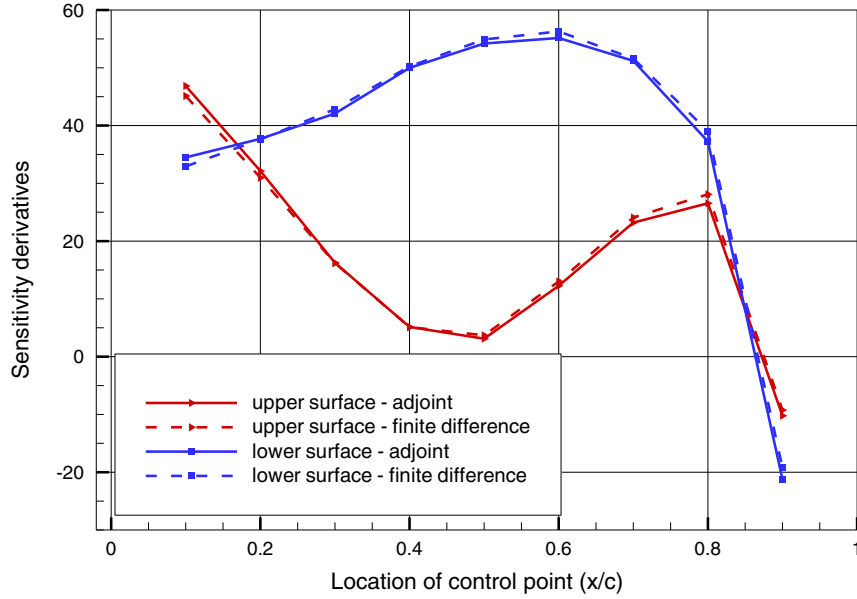**Fig. 13   FFD box and control points generated on NLF(1)-0416 airfoil.**
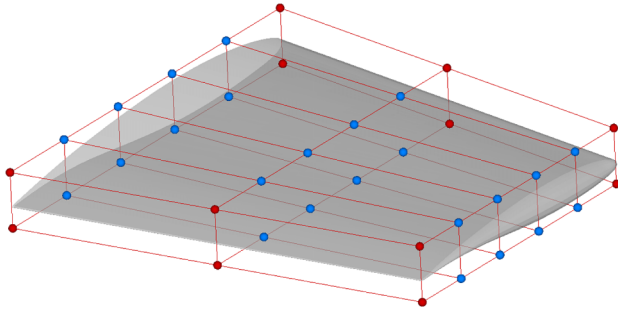
Fig. 14 Sensitivity derivatives.

Fig. 15 FFD box and control points (blue spheres depict the active control points).

less than 1% difference in the L_2 norm of the sensitivity derivatives computed by finite difference approximation. Based on these validation studies performed for two- and three-dimensional flows, it is

now concluded that the adjoint solver developed provides accurate sensitivity derivatives. Furthermore, the flow solver and the adjoint solver may be employed to perform two-dimensional and three-dimensional aerodynamic shape optimization studies for natural laminar flows.

C. Optimization Studies

Following the validation studies, the adjoint solver developed is now employed for the range parameter optimization of the NLF(1)-0416 airfoil and the endurance parameter optimization of the low-aspect-ratio wing.

1. Maximization of Range Parameter of NLF(1)-0416

In the first aerodynamic shape optimization case, the maximization of the range parameter (the ratio of c_l/c_d) for an NLF(1)-0416 airfoil is performed under the flow conditions of $M = 0.1$, $Re = 2 \times 10^6$, and $\alpha = 4.5$ deg, for which $c_l = 1.0$. The single-point optimization problem may be written as
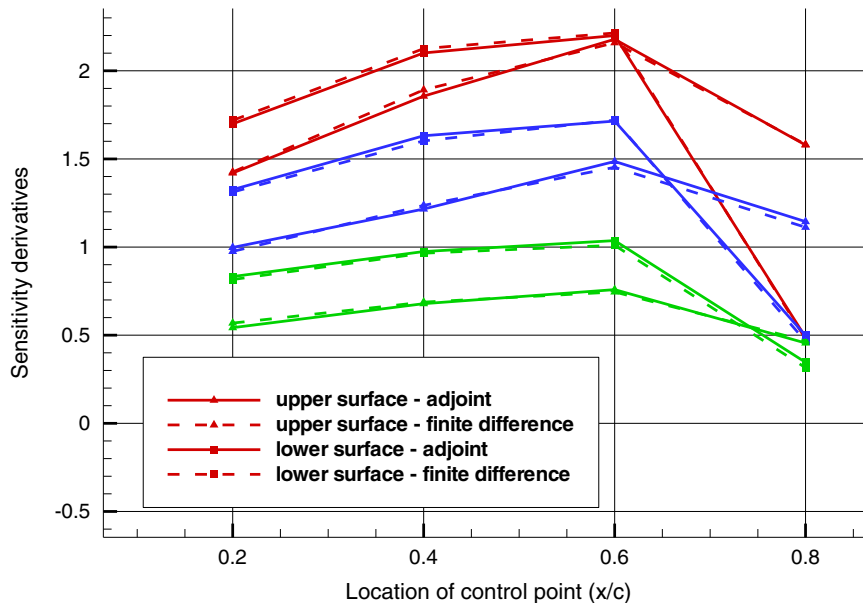

Fig. 16 Sensitivity derivatives computed by the finite difference and the adjoint method at the root chord (red), at the midspan chord (blue), and at the tip chord (green).

$$\max_{\boldsymbol{w}} I(\boldsymbol{w}) = c_l(\boldsymbol{w})/c_d(\boldsymbol{w}) \qquad (26)$$

where $\boldsymbol{w}$ refers to the y coordinates of the control points of the FFD box as the design variables. The same FFD box used in the validation study is again employed (Fig. 13). The movement of the control points is restrained by the half-FFD box thickness in order to prevent the emergence of infeasible profiles.

Figure 17 shows the evolution of the objective function and its components along the optimization steps driven by Dakota. The optimum design point is reached in five optimization steps.

Figure 18 shows the baseline and optimized airfoils. The corresponding pressure and skin-friction coefficients are given in Fig. 19. It is observed that the maximum thickness of the optimized profile is reduced, whereas its camber is increased slightly. As a result, the

optimized airfoil now has a higher suction pressure at the leading edge and a higher-pressure distribution along the lower airfoil surface. Thus, the lift increases, and the initial lift coefficient value of 1.0 goes up to a value of 1.116. Furthermore, the variation of the skin friction does not show a significant change, and the transition onset occurs at about the same location. The drag coefficient decreases slightly by about one drag count. As a result, the range parameter goes up from 117.3 to its maximum value of 132.8, which indicates about 13.2% improvement.

2. Maximization of Endurance Parameter of MDO 505 Wing

In this three-dimensional optimization case, the endurance parameter of the low-aspect-ratio MDO 505 wing considered in validation studies is optimized at a fixed angle of attack of 2.1 deg, $M = 0.15$,
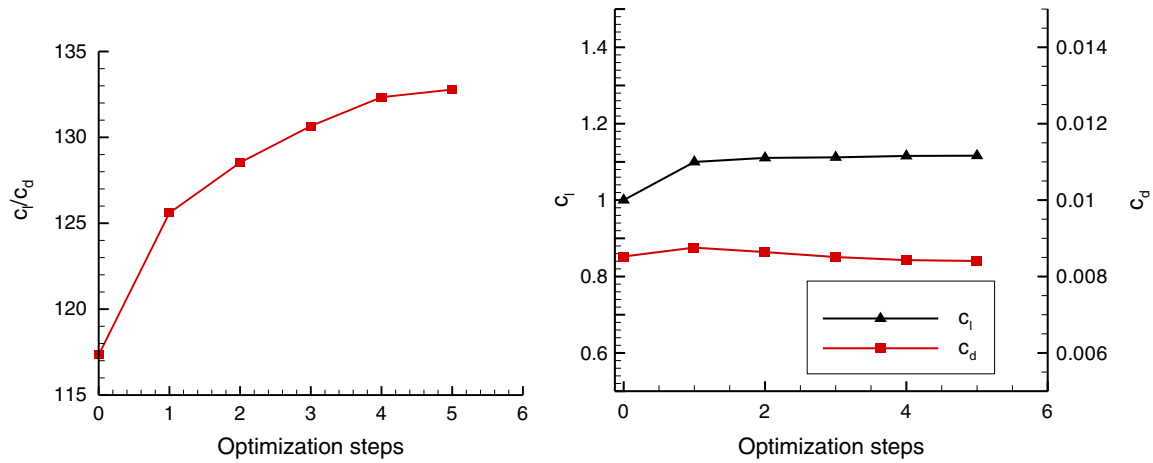

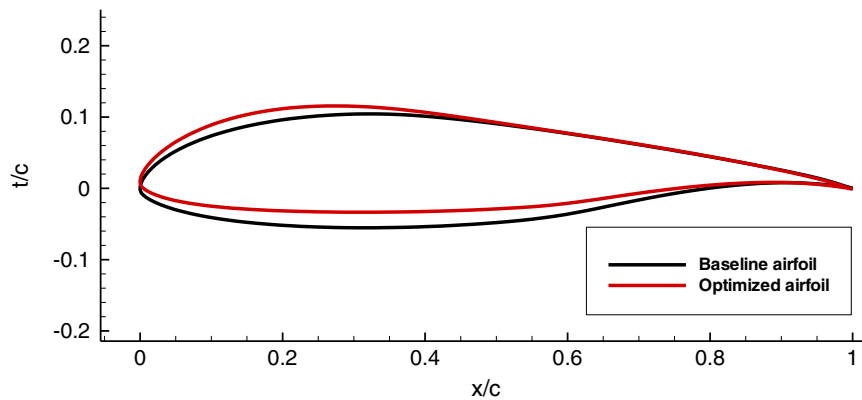**Fig. 17   Evolution of c_l/c_d throughout optimization steps.**

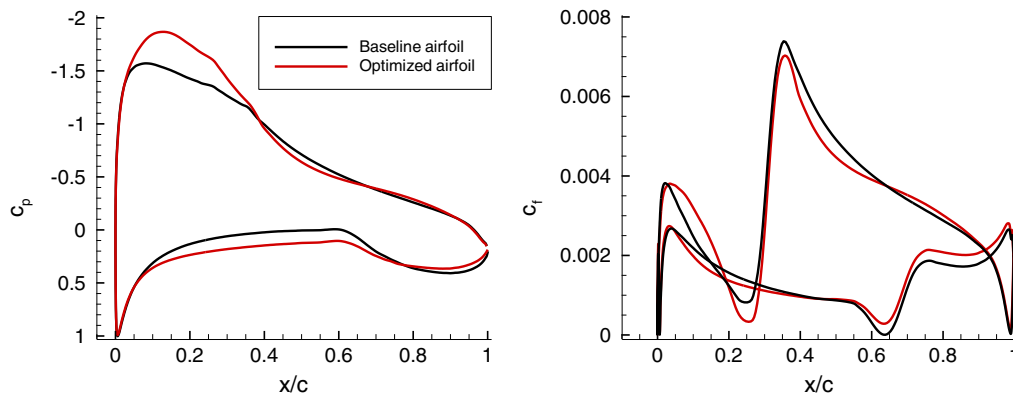**Fig. 18   The baseline and optimized profiles.**

Fig. 19   The pressure coefficient distributions of the baseline and the optimized profiles.
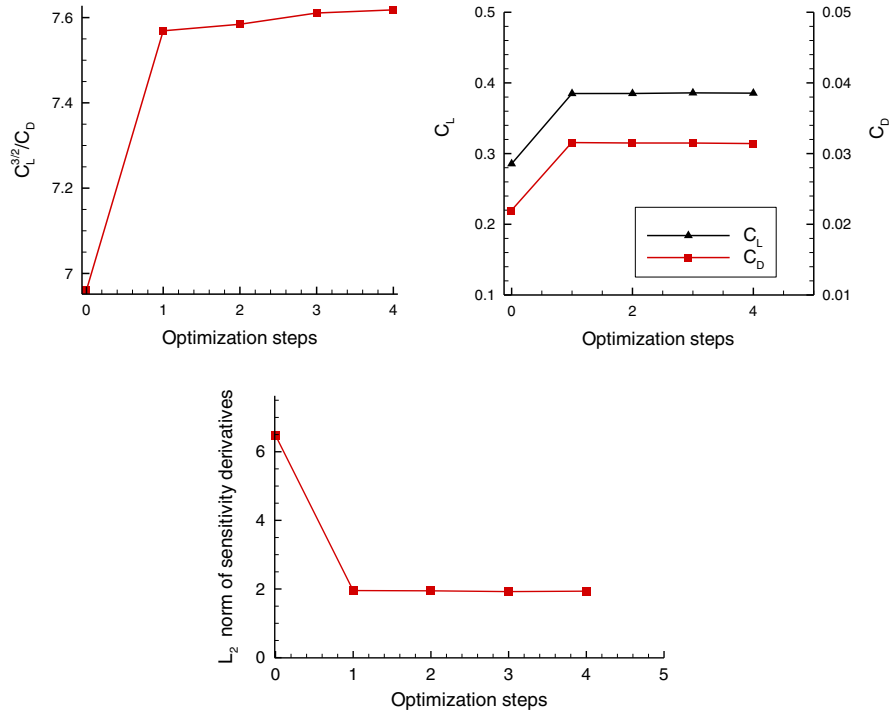
Fig. 20   Evolution of the endurance parameter and L_2 norm of the sensitivity derivatives.
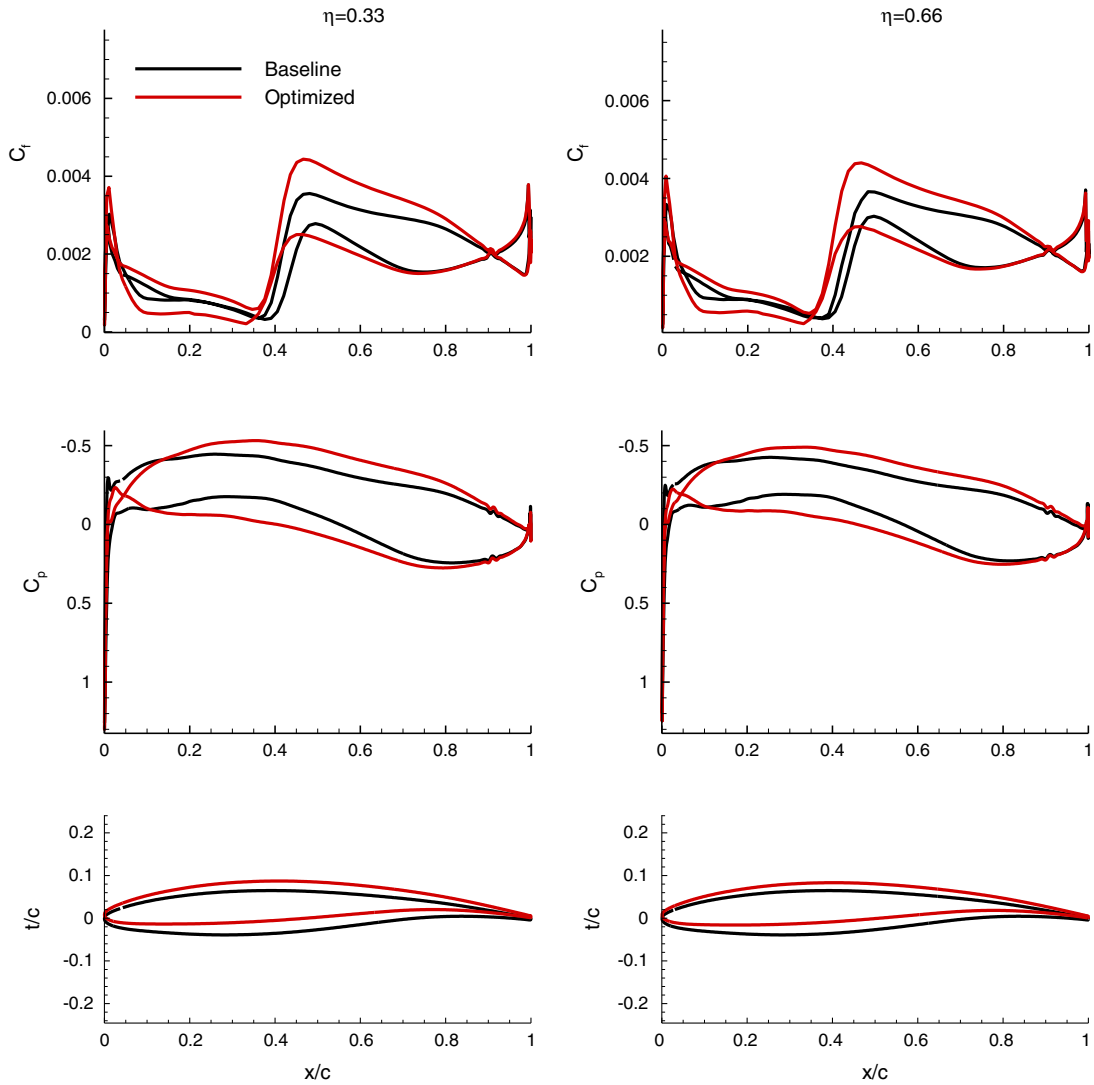

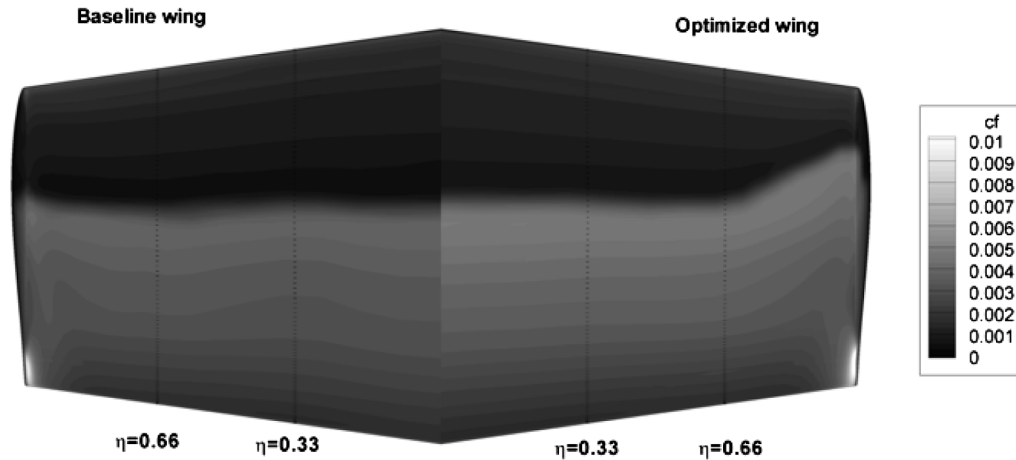Fig. 21   The wing sections of the baseline wing and the optimized wing.

Fig. 22   The skin-friction distribution on the upper surfaces of the baseline and the optimized wings.

and $Re = 3.4 \times 10^6$ per meter. The endurance parameter, which is taken as the objective function, is stated as

$$\max_{\boldsymbol{w}} I(\boldsymbol{w}) = C_L^{3/2}(\boldsymbol{w})/C_D(\boldsymbol{w}) \qquad (27)$$

where $\boldsymbol{w}$ similarly denotes the design variables of the problem. In the study, the same FFD box employed earlier is used again (Fig. 15). The FFD box has 36 control points: 24 of which are taken as the design variables. The maximum movement of the control points is restrained by the half-FFD box thickness.

The optimization process is similarly driven by the quasi-Newton algorithm available in Dakota. Figure 20 illustrates the evolution of the objective function and its components of C_L and C_D throughout the optimization steps. In this three-dimensional case, the optimization process converges within four optimization steps. Moreover, the reason for the L_2 norm not being reduced any further is that the thickness constraint is imposed. The constraint restrains some of the FFD box parameters and prevents the corresponding sensitivity derivative components from being reduced.

In Fig. 21, the change in the wing sections, the change in the distributions of the pressure coefficients, and the skin-friction coefficients are given in two spanwise stations. The optimized pressure distributions, which cause the lift to increase, have higher suction pressures due to the increased camber. The skin-friction distribution at $\eta = 0.33$ indicates that the transition onset location stays almost the same, whereas the skin-friction coefficient at $\eta = 0.66$ indicates a slightly earlier transition onset. Yet, there is no flow separation observed on the optimized wing.

Figure 22 shows the skin-friction distributions over the baseline and optimized wings. As observed, as the lift increases, the transition onset location on the optimized wing (and therefore the skin-friction drag) stays almost the same along the span before it retreats toward the wingtip due to the increasing effect of the tip vortices. As a result, the endurance parameter of the optimized wing is increased by 9.4%.

IV.   Conclusions

A discrete adjoint-based aerodynamic shape optimization framework for natural laminar flow is successfully developed. An in-house RANS solver is first equipped with the B-C transition model in order to predict the transition onset for natural laminar flows. Validation studies for natural laminar flows over airfoils and wings are successfully performed. It is also shown that the B-C transition model predicts the transition onset accurately and agrees well with the numerical and experimental studies.

An accompanying discrete adjoint solver is next developed for natural laminar flows. In the development of the adjoint solver, an automatic differentiation tool, TAPENADE, is used. The sensitivity derivatives computed by the adjoint solver are validated for two-dimensional and three-dimensional flows, which include laminar to

turbulent transition. The adjoint-based sensitivity derivatives are then used together with an open-source optimization tool, Dakota, to perform aerodynamic shape optimization studies. The optimization of the NLF(1)-0416 airfoil and a low-aspect-ratio wing are successfully performed. The range parameter of the NLF airfoil is increased by about 13.2%, and the endurance parameter of the wing is increased by about 9.4%.

References

[1] Fujino, M., Yoshizaki, Y., and Kawamura, Y., "Natural-Laminar-Flow Airfoil Development for a Lightweight Business Jet," *Journal of Aircraft*, Vol. 40, No. 4, 2003, pp. 609–615.
https://doi.org/10.2514/2.3145

[2] Fujino, M., "Design and Development of the Honda Jet," *Journal of Aircraft*, Vol. 42, No. 3, 2005, pp. 755–764.
https://doi.org/10.2514/1.12268

[3] Campell, R. L., Campell, M. L., and Streit, T., "Progress Toward Efficient Laminar Flow Analysis and Design," *29th AIAA Applied Aerodynamics Conference*, AIAA Paper 2011-3527, 2011.
https://doi.org/10.2514/6.2011-3527

[4] Crouch, J., "Boundary-Layer Transition Prediction for Laminar Flow Control (Invited)," *45th AIAA Fluid Dynamics Conference*, AIAA Paper 2015-2472, 2015.
https://doi.org/10.2514/6.2015-2472

[5] Lyu, Z., Xu, Z., and Martins, J. R. R. A., "Benchmarking Optimization Algorithms for Wing Aerodynamic Design Optimization," *Eighth International Conference on Computational Fluid Dynamics (ICCFD8)*, Paper ICCFD8-2014-0203, Chengdu, Sichuan, China, July 2014.
https://doi.org/10.1.1.664.9175

[6] Yu, Y., Lyu, Z., Xu, Z., and Martins, J. R. R. A., "On the Influence of Optimization Algorithm and Initial Design on Wing Aerodynamic Shape Optimization," *Aerospace Science and Technology*, Vol. 75, April 2018, pp. 183–199.
https://doi.org/10.1016/j.ast.2018.01.016

[7] Nemili, A., Özkaya, E., Gauger, G. R., Kramer, F., and Thiele, F., "Accurate Discrete Adjoint Approach for Optimal Active Separation Control," *AIAA Journal*, Vol. 55, No. 9, 2017, pp. 3016–3026.
https://doi.org/10.2514/1.J055009

[8] Dilgen, C. B., Dilgen, S. B., Fuhrman, D. R., Sigmund, O., and Lazarov, B. S., "Topology Optimization of Turbulent Flows," *Journal of Computer Methods in Applied Mechanics and Engineering*, Vol. 331, April 2018, pp. 363–393.
https://doi.org/10.1016/j.cma.2017.11.029

[9] Albring, T., Sagebaum, M., and Gauger, N. R., "Efficient Aerodynamic Design Using the Discrete Adjoint Method in SU2," *17th AIAA/ISSMO*

Multidisciplinary Analysis and Optimization Conference, AIAA Paper 2016-3518, 2016.
https://doi.org/10.2514/6.2016-3518

[10] Djeddi, R., and Ekici, K., "FDOT: A Fast, Memory-Efficient and Automated Approach for Discrete Adjoint Sensitivity Analysis Using the Operator Overloading Technique," *Aerospace Science and Technology*, Vol. 91, Aug. 2019, pp. 159–174.
https://doi.org/10.1016/j.ast.2019.05.004

[11] Khayatzadeh, P., and Nadarajah, S., "Aerodynamic Shape Optimization via Discrete Viscous Adjoint Equations for the $k - \omega$ SST Turbulence and $y - Re_\theta$ Transition Models," *49th AIAA Aerospace Sciences Meeting Including the New Horizons Forum and Aerospace Exposition*, AIAA Paper 2011-1247, 2011.
https://doi.org/10.2514/6.2011-1247

[12] Khayatzadeh, P., and Nadarajah, S., "Aerodynamic Shape Optimization of Natural Laminar Flow (NLF) Airfoils," *50th AIAA Aerospace Sciences Meeting Including the New Horizons Forum and Aerospace Exposition*, AIAA Paper 2012-0061, 2012.
https://doi.org/10.2514/6.2012-61

[13] Menter, F. R., Langtry, R. B., Likki, S. R., Suzen, Y. B., Huang, P. G., and Volker, S., "A Correlation-Based Transition Model Using Local Variables: Part I—Model Formulation," *Proceedings of the ASME Turbo Expo 2004: Power for Land, Sea, and Air*, Vol. 4, ASME, New York, June 2004, pp. 57–67.
https://doi.org/10.1115/GT2004-53452

[14] Rashad, R., and Zingg, D., "Aerodynamic Shape Optimization for Natural Laminar Flow Using a Discrete-Adjoint Approach," *AIAA Journal*, Vol. 54, No. 11, 2016, pp. 3321–3337.
https://doi.org/10.2514/1.J054940

[15] Yang, Z., and Mavriplis, D. J., "Discrete Adjoint Formulation for Turbulent Flow Problems with Transition Modelling on Unstructured Meshes," *AIAA SciTech 2019 Forum*, AIAA Paper 2019-0294, 2019.
https://doi.org/10.2514/6.2019-0294

[16] Coder, J. G., and Maughmer, M. D., "Computational Fluid Dynamics Compatible Transition Modeling Using an Amplification Factor Transport Equation," *AIAA Journal*, Vol. 52, No. 11, 2014, pp. 2506–2512.
https://doi.org/10.2514/1.J052905

[17] Lee, J. D., and Jameson, A., "Natural-Laminar-Flow Airfoil and Wing Design by Adjoint Method and Automatic Transition Prediction," *47th AIAA Aerospace Sciences Meeting Including the New Horizons Forum and Aerospace Exposition*, AIAA Paper 2009-0897, 2009.

[18] Pederson, C. C., Choudhari, M. M., Zhou, B. Y., Paredes, P., and Diskin, B., "Shape Optimization of Vortex Generators to Control Mack Mode Amplification," *AIAA Aviation 2020 Forum*, AIAA Paper 2020-2963, 2020.

[19] Cakmakcioglu, S. C., Bas, O., and Kaynak, U., "A Correlation-Based Algebraic Transition Model," *Journal of Mechanical Engineering Science*, Vol. 232, No. 21, 2018, pp. 3915–3929.
https://doi.org/10.1177/0954406217743537

[20] Hascoet, L., and Pascual, V., "The Tapenade Automatic Differentiation Tool: Principles, Model, and Specification," *ACM Transactions on Mathematical Software*, Vol. 39, No. 3, 2013, pp. 1–43.
https://doi.org/10.1145/2450153.2450158

[21] Adams, B. M., Bohnhoff, W. J., Dalbey, K. R., Ebeida, M. S., Eddy, J. P., Eldred, M. S., Geraci, G., Hooper, R. W., Hough, P. D., Hu, K. T., Jakeman, J. D., Khalil, M., Maupin, K. A., Monschke, J. A., Ridgway, E. M., Rushdi, A. A., Stephens, J. A., Swiler, L. P., Vigil, D. M., Wildey, T. M., and Winokur, J. G., *Dakota, A Multilevel Parallel Object-Oriented Framework for Design Optimization, Parameter Estimation, Uncertainty Quantification, and Sensitivity Analysis: Version 6.11 User's Manual*, Sandia National Laboratories, Albuquerque, NM, 2019.

[22] Nishikawa, H., and Kitamura, K., "Very Simple, Carbuncle-Free, Boundary-Layer-Resolving, Rotated-Hybrid Riemann Solvers," *Journal of Computational Physics*, Vol. 227, No. 4, 2008, pp. 2560–2581.
https://doi.org/10.1016/j.jcp.2007.11.003

[23] Harten, A., Lax, P. D., and van Leer, B., "On Upstream Differencing and Godunov-Type Schemes for Hyperbolic Conservation Laws," *SIAM Reviews*, Vol. 25, No. 1, 1983, pp. 35–61.

[24] Spalart, P., and Allmaras, S., "A One-Equation Turbulence Model for Aerodynamic Flows," *30th Aerospace Sciences Meeting and Exhibit*, AIAA Paper 1992-0439, 1992.
https://doi.org/10.2514/6.1992-439

[25] Kaya, H., "Development of a Discrete Adjoint-Based Aerodynamic Shape Optimization Tool for Natural Laminar Flows," Ph.D. Dissertation, Aerospace Engineering Dept., Middle East Technical Univ., Ankara, Turkey, 2020.

[26] Kosarev, L., Seror, S., and Lifshitz, Y., "Parabolized Stability Equations Code with Automatic Inflow for Swept Wing Transition Analysis,"

Journal of Aircraft, Vol. 53, No. 6, 2016, pp. 1647–1669.

[27] Halila, G. L. O., Chen, G., Shi, Y., Fidkowski, K. J., Martins, J. R. R. A., and de Mendonca, M. T., "High-Reynolds Number Transitional Flow Simulation via Parabolized Stability Equations with an Adaptive RANS Solver," *Aerospace Science and Technology*, Vol. 91, Aug. 2019, pp. 321–336.
https://doi.org/10.1016/j.ast.2019.05.018

[28] Menter, F. R., Smirnov, P. E., Liu, T., and Avancha, R., "A One-Equation Local Correlation-Based Transition," *Journal of Fluids Engineering*, Vol. 95, No. 4, 2015, pp. 583–619.
https://doi.org/10.1007/s10494-015-9622-4

[29] Walters, D. K., and Leylek, J. H., "A New Model for Boundary-Layer Transition Using a Single-Point RANS Approach," *Journal of Turbomachinery*, Vol. 126, No. 1, 2004, pp. 193–202.
https://doi.org/10.1115/1.1622709

[30] Nagapetyan, H., and Agarwal, R. K., "Development of a New Transitional Flow Model Integrating the Wray-Agarwal Turbulence Model with an Intermittency Transport Equation," *2018 Fluid Dynamics Conference, AIAA Aviation Forum*, AIAA Paper 2018-3384, 2018.
https://doi.org/10.2514/6.2018-3384

[31] Abu-Ghannam, B. J., and Shaw, R., "Natural Transition of Boundary Layers-The Effects of Turbulence, Pressure Gradient, and Flow History," *Journal of Mechanical Engineering Science*, Vol. 22, No. 5, 1980, pp. 213–228.
https://doi.org/10.1243/JMES_JOUR_1980_022_043_02

[32] Mayle, R. E., "The Role of Laminar-Turbulent Transition in Gas Turbine Engines," *Proceedings of the ASME 1991 International Gas Turbine and Aeroengine Congress and Exposition*, Vol. 5, ASME, New York, June 1991, p. V005T17A001.
https://doi.org/10.1115/91-GT-261

[33] Palacios, F. D., Economon, T. D., and Albring, T., the SU2 Contributors, "SU2—The Open-Source CFD Code (Version 6.1.0 'Falcon')," 2018, https://github.com/su2code/SU2/releases/tag/v6.1.0.

[34] Economon, T. D., Palacios, F., Copeland, S. R., Lukaczyk, T. W., and Alonso, J. J., "SU2: An Open-Source Suite for Multiphysics Simulation and Design," *AIAA Journal*, Vol. 54, No. 3, 2016, pp. 828–846.
https://doi.org/10.2514/1.j053813

[35] Cakmakcioglu, S. C., Bas, O., Mura, R., and Kaynak, U., "A Revised One-Equation Transitional Model for External Aerodynamics," *AIAA Aviation 2020 Forum*, AIAA Paper 2020-2706, 2020.

[36] Mura, R., and Cakmakcioglu, S. C., "A Revised One-Equation Transitional Model for External Aerodynamics—Part I: Theory, Validation and Base Cases," *AIAA Aviation 2020 Forum*, AIAA Paper 2020-2714, 2020.

[37] Griewank, A., and Walther, A., *Evaluating Derivatives: Principles and Techniques of Algorithmic Differentiation*, 2nd ed., SIAM, Philadelphia, 2008.

[38] Naumann, U., *The Art of Differentiating Computer Programs: An Introduction to Algorithmic Differentiation*, SIAM, Philadelphia, 2011.
https://doi.org/10.2514/1.29123

[39] Mader, C. A., Martins, J. R. R. A., Alonso, J. J., and van der Weide, E., "ADjoint: An Approach for the Rapid Development of Discrete Adjoint Solvers," *AIAA Journal*, Vol. 46, No. 4, 2008, pp. 863–878.
https://doi.org/10.2514/1.29123

[40] Lyu, Z., Kenway, G. K. W., Paige, C., and Martins, J. R. R. A., "Automatic Differentiation Adjoint of the Reynolds-Averaged Navier–Stokes Equations with a Turbulence Model," *21st AIAA Computational Fluid Dynamics Conference*, AIAA Paper 2013-2581, 2013.
https://doi.org/10.2514/6.2013-2581

[41] Amestoy, P. R., Duff, I. S., L'excellent, J., and Koster, J., "A Fully Asynchronous Multifrontal Solver Using Distributed Dynamic Scheduling," *SIAM Journal on Matrix Analysis and Applications*, Vol. 23, No. 1, 2001, pp. 15–41.

[42] Amestoy, P. R., Buttari, A., L'excellent, J.-Y., and Mary, T., "Performance and Scalability of the Block Low-Rank Multifrontal Factorization on Multicore Architectures," *ACM Transactions on Mathematical Software*, Vol. 45, No. 1, 2019, pp. 2:1–2:26.
https://doi.org/10.1137/s0895479899358194

[43] Balay, S., Gropp, W. D., McInnes, L. C., and Smith, B. F., "Efficient Management of Parallelism in Object Oriented Numerical Software Libraries," *Modern Software Tools in Scientific Computing*, edited by E. Arge, A. M. Bruaset, and H. P. Langtangen, Birkhauser Press, Boston, MA, 1997, pp. 163–202.

[44] Balay, S., Abhyankar, S., Adams, M. F., Brown, J., Brune, P., Buschelman, K., Dalcin, L., Dener, A., Eijkhout, V., Gropp, W. D., Karpeyev, D., Kaushik, D., Knepley, M. G., May, D. A., McInnes, L. C., Mills, R. T., and Munson, T., PETSc: Portable, Extensible Toolkit for Scientific Computation (Version 3.11.3), 2019, https://petsc.org/release/download/.

[45] Balay, S., Abhyankar, S., Adams, M. F., Brown, J., Brune, P., Buschelman, K., Dalcin, L., Dener, A., Eijkhout, V., Gropp, W. D., Karpeyev, D., Kaushik, D., Knepley, M. G., May, D. A., McInnes, L. C., Mills, R. T., Munson, T., Rupp, K., Sanan, P., Smith, B. F., Zampini, S., and Zhang, H., "PETSc Users Manual," Tech. Rept. ANL-95/11, Rev 3.11, Argonne National Laboratory, Illinois, 2019.

[46] Samareh, J., "Aerodynamic Shape Optimization Based on Free-Form Deformation," *10th AIAA/ISSMO Multidisciplinary Analysis and Optimization Conference*, AIAA Paper 2004-4630, 2004.
https://doi.org/10.2514/6.2004-4630

[47] Dwight, R. P., "Robust Mesh Deformation Using the Linear Elasticity," *Computational Fluid Dynamics 2006: Proceedings of the Fourth International Conference on Computational Fluid Dynamics, ICCFD4*, edited by H. Deconinck, and E. Dick, Springer, Berlin, 2009, pp. 401–406.

[48] Broyden, C. G., "A New Double-Rank Minimization Algorithm," *AMS Notices*, Vol. 16, 1969, Paper 670.

[49] Fletcher, R., "A New Approach to Variable Metric Algorithms," *Computer Journal*, Vol. 13, No. 3, 1970, pp. 317–322.
https://doi.org/10.1093/comjnl/13.3.317

[50] Goldfarb, D., "A Family of Variable-Metric Methods Derived by Variational Means," *Mathematics of Computation*, Vol. 24, No. 109, 1970, pp. 23–26.
https://doi.org/10.2307/2004873

[51] Shanno, D. F., "On Variable-Metric Methods for Sparse Hessians," *Mathematics of Computation*, Vol. 34, No. 150, 1980, pp. 499–514.
https://doi.org/10.2307/2006098

[52] Meza, J. C., Olivia, R. A., Hough, P. D., and Williams, P. J., "OPT++: An Object-Oriented Toolkit for Nonlinear Optimization," *ACM Transactions on Mathematical Software*, Vol. 33, No. 2, 2007, Paper 12.
https://doi.org/10.1145/1236463.1236467

[53] Somers, D. M., "Design and Experimental Results for a Natural-Laminar-Flow Airfoil for General Aviation Applications," NASA Langley Research Center, NASA TP-1861, Hampton, VA, 1981.

[54] Kammegne, M. J. T., Botez, R. M., Manou, M., and Mebarki, Y., "Experimental Wind Tunnel Testing of a New Multidisciplinary Morphing Wing Model," *Advances in Mathematics and Computer Science and their Applications*, WSEAS Press, Jan. 2016, pp. 90–97.

[55] Koreanschi, A., Gabor, O. S., Acotto, J., Brianchon, G., Portier, G., Botez, R. M., Mamou, M., and Mebarki, Y., "Optimization and Design of an Aircraft's Morphing Wing-Tip Demonstrator for Drag Reduction at Low Speed, Part II—Experimental Validation Using Infra-Red Transition Measurements During Wind Tunnel Tests," *Chinese Journal of Aeronautics*, Vol. 30, No. 1, 2017, pp. 164–174.
https://doi.org/10.1016/j.cja.2016.12.018

K. E. Willcox
Associate Editor